High Resolution Near-Field Electromagnetic Holography for Dynamic Source Identification in Underwater Mediums

Hatim F. Alqadah[1, *], Nicolas P. Valdivia[2], and Earl G. Williams[3]

Abstract—This paper investigates the source reconstruction problem in underwater mediums using a compressive Near-Field Electromagnetic Holography (NEH) approach. More specifically we investigate the use of ℓ_1 regularization for the purpose of decomposing near-field magnetic and/or electric surface measurements into electric and magnetic dipole sources. Our study indicates that not only do ℓ_1 decompositions enable much higher resolution of sources than traditional ℓ_2 approaches, but important features of the dipoles are preserved in the reconstruction. Our hypothesis are supported by numerical experiments as well as underwater physical measurements obtained in an earth field simulator facility.

1. INTRODUCTION

Source reconstruction of alternating current (AC) radiation sources have a wide application in civilian and military marine based electromagnetics. Inverse source reconstruction techniques rely on obtaining electric and/or magnetic field measurements away from a radiating source, and then mathematically back-projecting the fields to obtain a relevant source model. If successful, not only can the electromagnetic field be accurately predicted throughout an entire volume, but also important features such as location and distribution of the source currents can be identified. The latter benefit can provide important information to assist with automated diagnosis of radiation anomalies. While traditional work in underwater electromagnetics has primarily focused on magneto-static fields (DC fields) arising from interactions between the ferromagnetic steel portions of the ship and Earth's magnetic field, characterizing underwater AC sources within the Extremely Low Frequency (ELF) (1–200 Hz) using magnetic and even electric field measurements has received recent interest. Examples of possible AC sources include cathodic related currents, roll-induced eddy currents, electric generators, and on-board electronic equipment [10].

One key measure of success in source reconstruction imaging is resolution. The ability to resolve sources far below the diffraction limit of $\lambda/2$ is known as super-resolution. In the ELF band the wavelength of the radiating fields can be on the order of kilometers (see Figure 1). Clearly then super-resolution is absolutely critical to be of any practical use in underwater applications. Near-Field Electromagnetic Holography (NEH) is one such source reconstruction method allowing for super-resolution of sources. NEH back-projects measured field data recorded on a surface (a hologram) located in the near-field, but far enough from the radiation source so that the measuring sensors do not perturb the "true" fields. Similar to Near-Field Acoustic holography (NAH) where Williams [19, 20] demonstrated that super-resolution of the technique can be attributed to the wealth of information provided by evanescent super-sonic propagation modes captured in near-field holograms. In the far-field these modes would have long vanished and cannot be recovered. For underwater mediums, due to the large wavelengths involved, measurement sensors can be positioned in the near-field region without any risk of interacting with the radiation source. This makes NEH very well suited for super-resolving

* Corresponding author: Hatim F. Alqadah (hatim.alqadah.ctr@nrl.navy.mil).
[1] NRC Postdoctoral Associate, Washington, D.C., USA. [2] Code 7130, Naval Research Laboratory, Washington, D.C., USA. [3] Code 7106 Naval Research Laboratory, Washington D.C., USA.
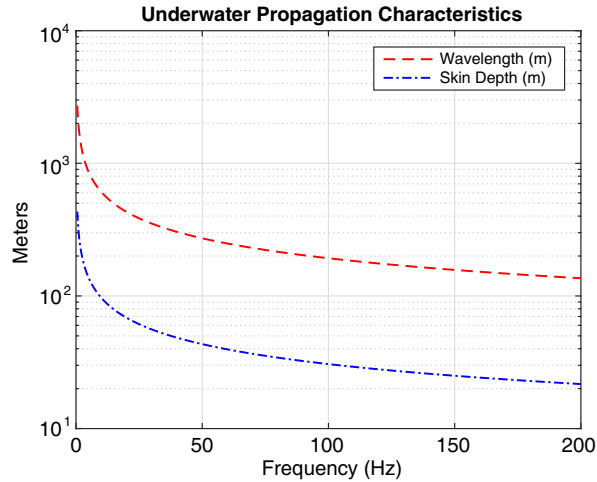
Figure 1. Plot of wavelength and skin-depth in conductive underwater mediums on the frequency band 1–200 Hz.

and characterizing underwater sources. However in practice, stability issues can severely limit the quality of the inversion in terms of accuracy and resolution. Firstly, it is important to realize that an electromagnetic back-projection problem is almost always under-determined and hence non-unique [15]. Generally, the reconstructed current sources are simply an intermediary mathematical construct used to provide an equivalent description of the radiated field. Therefore a particular solution does not necessarily have a physical interpretation [2]. In certain cases however, a physically relevant solution may exist, especially when the source surface is chosen to coincide with a material discontinuity. Without imposing explicit constraints on the back-projection problem, there is no reason that such a solution should be chosen over other possible candidates. Secondly, the evanescent radiating components also act as noise amplifiers during inversion which often results in poorly constructed solutions if not properly mitigated. The prevalent approach for these two issues is by means of ℓ_2 based regularization. As explained in [8] generally ℓ_2 regularization approaches are either obtained through direct means, i.e., explicitly solving a Tikhonov regularization problem, or by means of semi-convergence of iterative solvers such as the conjugate-gradient (CG) method. Recent works in underwater NEH include Morgan [12] and Williams [21] both of whom employed ℓ_2 regularized k-space techniques for the back-projection. Valdivia and Williams [17] considered underwater NEH for arbitrarily shaped geometries by means of an equivalent magnetic current formulation and a special iterative LSQR solver that determined an optimal stopping point. In non-conductive media (free space) [15] also addressed the non-uniqueness issue of source reconstruction by imposing an explicit constraint in order to explicitly reconstruct Love's (zero interior fields) equivalent currents. Regularization in that work was imposed by means of CG iteration. While the previous works in underwater NEH mentioned above have shown a successful ability to extrapolate the field away from the source, the attainable resolution of ℓ_2 methods in underwater applications is quite poor, and often times fails to adequately localize a particular source. This is due to the fact that ℓ_2 methods must compromise on resolution in exchange for stability. Furthermore as we will demonstrate in this paper the current sources reconstructed by ℓ_2 methods are unable to reconstruct the physical nature of the source, which could provide valuable source of information for diagnostic applications.

In this work we seek to employ a compressive sensing approach to underwater NEH. Compressive approaches rely on the ability to recover signals *known a priori to be sparse* with respect to some chosen basis. In AC underwater applications the size of the source current distributions are often quite small relative to the surface of interest, and thus a sparsity prior is justifiable. Previous work by the authors [1] proposed a compressive NEH approach based on ℓ_1 regularization for non-conductive mediums. In that work it was established that ℓ_1 reconstructions exhibited far more localized representations of the sources than ℓ_2 approaches. In this paper we show that a compressive approach provides superior resolution of sources for underwater mediums relative to ℓ_2 approaches. We also demonstrate that the ℓ_1 approach

is able to ascertain the physical nature of the sources whereas an ℓ_2 approach will generally fail to do so. More specifically, for radiation due to an electric and/or magnetic dipole, only the ℓ_1 reconstruction provides the dipole location, polarity and type (electric or magnetic) with a high degree of accuracy. This observation can be related to the fact that explicitly seeking a sparse solution to an under-determined system provides for a better posed problem. For example the results of [5] show that under-determined systems satisfying certain technical requirements will in fact admit a unique solution if the underlying solution was indeed sparse. In the case of noisy data, [4] showed that a sparse solution can be recovered with over-whelming probability. In what follows, we first formulate the back-projection problem in Section 2. We then discuss our compressive approach in more detail in Section 3. In Section 4 we introduce a series of simple numerical experiments to verify our claims on the advantages of an ℓ_1 approach. In Section 5 we consider a further proof-of-concept using a series of physical experiments where magnetic sensor array data was taken in an Earth Field Simulator (EFS) experimental facility. We demonstrate a plane-to-plane reconstruction which accurately resolves and reconstructs small coil sources located within the interior of the vessel in question. Finally we conclude the paper with some final remarks in Section 6.

2. FORMULATION

Formulation of the inverse source problem is summarized in Figure 2(a). Here we define the interior region Ω_- with boundary Γ_s which is assumed to encompass all possible radiation sources. The exterior region labeled as Ω_+ represents an unbounded underwater medium which is free of any source currents or charges. As shown in Figure 2(a), generally the interior and exterior regions are comprised of different electromagnetic material parameters and the surface Γ_s is chosen to align with this discontinuity. In the exterior region it is assumed that we can macroscopically describe the background material with a scalar electric permittivity $\tilde{\epsilon} > 0$, a scalar magnetic permeability $\mu > 0$, and a scalar electric conductivity $\sigma \geq 0$. For a time-harmonic field with angular frequency ω we can conveniently define the effective electric permittivity in Ω_+ as $\epsilon = \tilde{\epsilon} + i\sigma/\omega$. According to the assumptions stated above, the exterior fields are divergence free and obey the homogeneous equations

$$\vec{\nabla} \times \vec{E}_+ - i\omega\mu\vec{H}_+ = 0, \quad \vec{\nabla} \times \vec{H}_+ + i\omega\epsilon\vec{E}_+ = 0, \tag{1}$$

where $e^{-i\omega t}$ time dependence is suppressed, and both $\vec{E}_+$ and $\vec{H}_+$ are assumed to be radiating solutions [6]. To uniquely determine the external fields the boundary values of the internal fields $\vec{E}'_-$ and $\vec{H}'_-$ must be determined. Invoking the field equivalence theorem [9], where as shown in Figure 2(b), we remove all original sources and materials in Ω_- and replace them with surface electric and magnetic currents $\vec{J}_s$ and $\vec{M}_s$. The external fields $\vec{E}_+$, $\vec{H}_+$ remain unchanged while the internal

(a) Original problem   (b) Equivalent problem
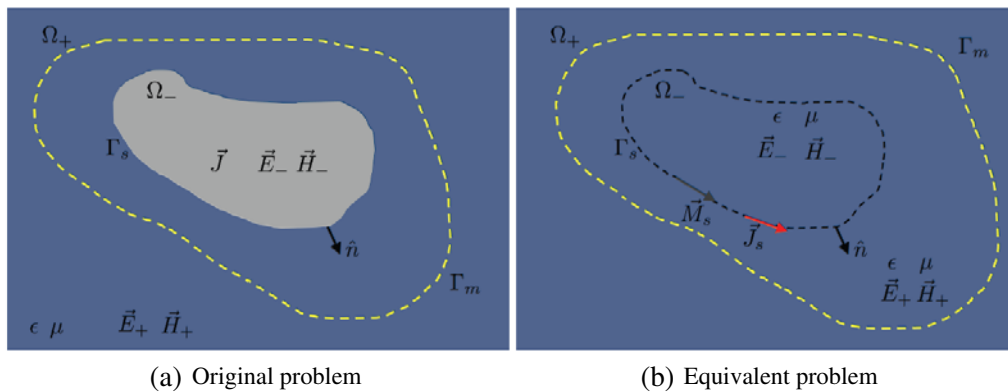
Figure 2. Here we show how the original problem (a) where all the sources are contained within the volume Ω_-. The problem is equivalent to (b) where volume sources are replaced with surface currents and the entire region is described with single constant propagation parameters.

fields are substituted with another set of fields $\vec{E}_-$, $\vec{H}_-$, which are related by the boundary conditions

$$\hat{n} \times \left[\vec{H}_+ - \vec{H}_- \right] = \vec{J}_s,$$
$$\hat{n} \times \left[\vec{E}_+ - \vec{E}_- \right] = \vec{M}_s. \tag{2}$$

With all volume sources and material discontinuities removed, both the external and internal fields can be represented by means of vector potentials,

$$\vec{H} = \vec{\nabla} \times \vec{A} + \frac{1}{i\omega\mu}\vec{\nabla} \times \vec{\nabla} \times \vec{F} \tag{3}$$

$$\vec{E} = \vec{\nabla} \times \vec{F} - \frac{1}{i\omega\epsilon}\vec{\nabla} \times \vec{\nabla} \times \vec{A}, \tag{4}$$

where the potentials are excited by the equivalent surface currents as

$$\vec{A}(\vec{x}) = \int_{\Gamma_s} \vec{J}_s(\vec{y})G(\vec{x},\vec{y})ds(\vec{y}) \tag{5}$$

$$\vec{F}(\vec{x}) = \int_{\Gamma_s} \vec{M}_s(\vec{y})G(\vec{x},\vec{y})ds(\vec{y}). \tag{6}$$

The scalar function $G(\vec{x},\vec{y})$ is the Helmholtz Green's function for an unbounded background medium

$$G(\vec{x},\vec{y}) = \frac{e^{ik|\vec{x}-\vec{y}|}}{4\pi|\vec{x}-\vec{y}|}, \tag{7}$$

where the complex-valued wavenumber k is given by the relation $k^2 = \omega^2\epsilon\mu$. We define projection operators $\mathcal{K}_{\Gamma_s\to\Gamma_m}$ and $\mathcal{L}_{\Gamma_s\to\Gamma_m}$ operating on an arbitrary surface current density $\vec{\Psi}$ on Γ_s as

$$\left(\mathcal{K}_{\Gamma_s\to\Gamma_m}\right)(\vec{\Psi})(\vec{x}) := \vec{\nabla} \times \int_{\Gamma_s} \vec{\Psi}(\vec{y})G(\vec{x},\vec{y})ds(\vec{y}), \quad \text{for } \vec{x} \in \Gamma_m, \tag{8}$$

$$\left(\mathcal{L}_{\Gamma_s\to\Gamma_m}\right)(\vec{\Psi})(\vec{x}) := \vec{\nabla} \times \vec{\nabla} \times \int_{\Gamma_s} \vec{\Psi}(\vec{y})G(\vec{x},\vec{y})ds(\vec{y}), \quad \text{for } \vec{x} \in \Gamma_m. \tag{9}$$

Given exterior electromagnetic field measurements $(\vec{E}_+^m, \vec{H}_+^m)$ on Γ_m, we can obtain the source currents responsible for radiating the exterior fields by solving the combined back-projection problem,

$$\begin{bmatrix} \vec{H}_+^m \\ \vec{E}_+^m \end{bmatrix} = \begin{bmatrix} \mathcal{K}_{\Gamma_s\to\Gamma_m} & \frac{1}{i\omega\mu}\mathcal{L}_{\Gamma_s\to\Gamma_m} \\ \frac{1}{i\omega\epsilon}\mathcal{L}_{\Gamma_s\to\Gamma_m} & \mathcal{K}_{\Gamma_s\to\Gamma_m} \end{bmatrix} \begin{bmatrix} \vec{J}_s \\ \vec{M}_s \end{bmatrix}. \tag{10}$$

It is not difficult to show that even when $\sigma > 0$ (10) does not yield a unique solution. To show this, consider setting the electric current density to zero which leaves an expansion only in terms of a single magnetic current. It can be shown (Theorem 2.2 in [17]) that under such premises current a unique solution radiating the observed field does exist. However by setting the magnetic current to zero and applying the same arguments one can show that an equivalent electric current can also radiate the same field. Hence we see that there is a null space associated with the combined back-projection operator, and the choice of interior fields will constitute a degree of freedom that impacts the physical meaning of the reconstructed currents.

We proceed to approximate the surface integrals in Eq. (10) over the currents by a finite sum of electric and magnetic dipoles (see [1] for details),

$$\vec{E}(\vec{x}) = \sum_{i=1}^{n_s} \vec{\nabla} \times \vec{m}_i G(\vec{x},\vec{y}_i) - \frac{1}{i\omega\mu}\sum_{i=1}^{n_s} \vec{\nabla} \times \vec{\nabla} \times \vec{e}_i G(\vec{x},\vec{y}_i),$$
$$\vec{H}(\vec{x}) = \sum_{i=1}^{n_s} \vec{\nabla} \times \vec{e}_i G(\vec{x},\vec{y}_i) + \frac{1}{i\omega\epsilon}\sum_{i=1}^{n_s} \vec{\nabla} \times \vec{\nabla} \times \vec{m}_i G(\vec{x},\vec{y}_i), \tag{11}$$

where $\vec{e}_i$ and $\vec{m}_i$ are electric and magnetic dipole moments at position $\vec{y}_i$. Given n_m tri-axial measurements of the magnetic and/or electric fields at the points $\{x_i\}_{i=1}^{n_m} \subset \Gamma_m$. Expressing the vector data in stacked form, i.e.,

$$\mathbf{E}_m = \begin{bmatrix} \mathbf{E}_x \\ \mathbf{E}_y \\ \mathbf{E}_z \end{bmatrix}, \quad \mathbf{H}_m = \begin{bmatrix} \mathbf{H}_x \\ \mathbf{H}_y \\ \mathbf{H}_z \end{bmatrix}, \tag{12}$$

yields the discretized back-projection problem

$$\begin{bmatrix} \mathbf{K}_{\Gamma_s \to \Gamma_m} & \dfrac{1}{i\omega\mu}\mathbf{L}_{\Gamma_s \to \Gamma_m} \\ \dfrac{1}{i\omega\epsilon}\mathbf{L}_{\Gamma_s \to \Gamma_m} & \mathbf{K}_{\Gamma_s \to \Gamma_m} \end{bmatrix} \begin{bmatrix} \mathbf{e} \\ \mathbf{m} \end{bmatrix} = \begin{bmatrix} \mathbf{H}_m \\ \mathbf{E}_m \end{bmatrix}. \tag{13}$$

The reason against using higher order elements in the discretization is primarily due to the fact that measurement noise tends to dominate over any errors introduced by finite discretization. As shown in [18] for the acoustic case, higher order elements do not contribute significantly to inversion performance. Thus using such a simple discretization allows for fast assembly times with minimal compromise on accuracy.

3. COMPRESSIVE APPROACH

For the sake of notational simplicity we can succinctly write (13) as the system

$$\mathbf{A}\mathbf{x} = \mathbf{b}. \tag{14}$$

Here the $m \times n$ matrix $\mathbf{A}$ is almost always rectangular ($m \ll n$), and our aim is to recover the amplitudes and orientations of the dipole sources encoded in $\mathbf{x}$, with the assumption that $\mathbf{x}$ is sparse. While a thorough discussion of compressive sensing is beyond the scope of this article, we want to highlight a few thoughts[†] concerning reconstruction of sparse solutions. It is well known that a brute force[†] computation of sparse solutions is a NP-hard hard problem [13], which is infeasible for our purposes. Over the years however, the area compressive sensing has experienced rapid development due to the emergence of methods that allow for sparse solutions to be found in polynomial time. This comes at the expense of relaxing the sparsity constraint a bit. The first category of such methods are known as greedy methods such as Orthogonal Matching Pursuit (OMP). Such methods have been recently been employed in radiation modeling applications (for example see [11]). The other approach is to consider a solution to the ℓ_1 problem,

$$\min_{\mathbf{x} \in \mathbb{C}^n} \frac{1}{2}\|\mathbf{A}\mathbf{x} - \mathbf{b}\|_2^2 + \alpha\|\mathbf{x}\|_1, \tag{15}$$

for an appropriately chosen $\alpha > 0$ which controls the balance between data fidelity and sparsity. In certain cases solutions (15) are either identical or close enough to sparse solutions computed by brute force, and provide the best convex sparse approximation. While greedy methods like OMP can be seen as a heuristic equivalent of (15), in many instances they fail to produce adequate sparse solutions in comparison to solutions of (15). This is particularly the case when the matrix $\mathbf{A}$ is ill-conditioned [7]. Thus greedy methods do not provide the level of robustness that is needed for NEH applications. Rather we choose to directly compute a solution to (15) by means of an Accelerated Proximal Gradient (APG)method which involves the following iterative process:

$$\mathbf{y}^{(n)} = \gamma\mathbf{x}^{(n)} + (1 - \gamma)\mathbf{x}^{(n-1)} \tag{16}$$

$$\mathbf{x}^{(n+1)} = \text{Shrink}\left(\mathbf{x}^{(n)} - \tau\mathbf{A}^H\left(\mathbf{A}\mathbf{y}^{(n)} - \mathbf{b}\right), \tau\alpha\right), \quad \text{for} \quad n = 1, \ldots, \tag{17}$$

where the shrinkage operator is defined component-wise, i.e., the ith component is computed as

$$(\text{Shrink}(\mathbf{z}, \mu))_i = \text{sgn}(z_i)\max\{|z_i| - \mu, 0\}. \tag{18}$$

and the parameter γ provides a linear combination of past estimates before computing a descent direction. APG methods are well suited for large-scale systems and also provide considerably faster

---

[†] This involves an ℓ_0 constraint on the vector $\mathbf{x}$.

convergence rates when matrix $\mathbf{A}$ is highly ill-conditioned (hence the name accelerated) than standard proximal gradient approaches. We employ a particular APG method known as Fast Iterative Shrinkage Thresholding Algorithm (FISTA) [3] which provides for a specific choice of γ. We summarize our numerical approach in algorithm 1.

**Algorithm 1** A particular APG algorithm known as FISTA.

---

    function APG_FISTA($\mathbf{A}, \mathbf{b}, \alpha$)
        $L \leftarrow \sigma_1(\mathbf{A}^H\mathbf{A})$ $\triangleright$ σ_1: spectral radius
        $\tau \leftarrow 1/L$
        $\mathbf{y}^{(0)} \leftarrow 0$
        $\mathbf{x}^{(0)} \leftarrow 0$
        for $n \leftarrow 0$ to $n_{\max}$ **do**
            $\mathbf{r}^{(n)} \leftarrow \mathbf{A}\mathbf{y}^{(n)} - \mathbf{b}$
            $\mathbf{x}^{(n+1)} \leftarrow \text{Shrink}\left(\mathbf{y}^{(n)} - \tau\left(\mathbf{A}^H\mathbf{r}^{(n)} - \alpha\mathbf{y}^{(n)}\right), \tau\alpha\right)$
            if $\frac{\|\mathbf{x}^{(n+1)}-\mathbf{x}^{(n)}\|_2}{\max\{\|\mathbf{x}^{(n+1)}\|_2, 1\}} < \text{tol}$ **then** break
            else
                $t^{(n+1)} \leftarrow \frac{1+\sqrt{1+4t^{(n)2}}}{2}$
                $\mathbf{y}^{(n+1)} \leftarrow \mathbf{x}^{(n+1)} + \frac{t^{(n)}}{t^{(n+1)}}(\mathbf{x}^{(n+1)} - \mathbf{x}^{(n)})$
            end if
        end for
        return $\mathbf{x}^{(n+1)}$
    end function

---

4. NUMERICAL EXPERIMENTS

In this section we conduct a series of simple plane-to-plane back-projection experiments in order to gain some insight into the ℓ_1 regularization approach. The experiments were focused on reconstructing two closely spaced dipole sources located on a plane 16 m above a measurement plane where the magnetic field will be measured. More precisely, both the source and measurement planes were oriented with their normals along the Z axis and truncated to have dimensions of 120 m in length (X axis) and 30 m

(a) 4 m depth   (b) 16 m depth
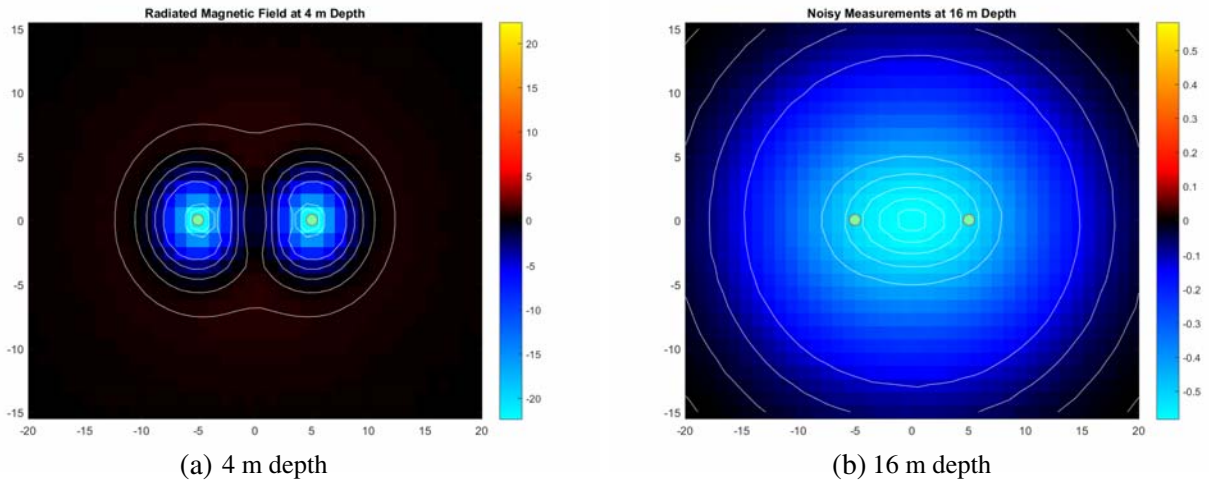
Figure 3. Visualizing the real part of magnetic field data generated by the sources in experiment 1 on observation planes at 4 m and 16 m depth respectively. The yellow dots indicate the exact positioning of the magnetic dipole sources on the source plane (0 m depth).

in width (Y axis). The source surface was located at zero depth ($z = 0$) and the measurement plane was located at a depth of $16\,\mathrm{m}$ ($z = -16$). The dipoles were then placed within $\delta\,\mathrm{m}$ of each other along the X axis, where we varied δ across the experiments. Magnetic field data resulting from the two dipoles was numerically computed for a frequency of $5\,\mathrm{Hz}$ and approximately 1% white Gaussian noise was added to each tri-axial channel. Both the measurement and source planes were sampled every $1\,\mathrm{m}$ in both the X and Y directions. Figure 3 shows an example of the placement of the two sources. Here the positioning of the two magnetic dipole sources used in experiment 1 are super-imposed on a plot of the real part of the magnetic field data at depths of $4\,\mathrm{m}$ and $16\,\mathrm{m}$ respectively. A similar setup was used for the remainder of the experiments. For under-water propagation parameters, we chose $\epsilon' = 80\epsilon_0\,\mathrm{F/m}$ as the relative dielectric constant, $\mu = \mu_0$, and a conductivity of $\sigma = 2.7\,\mathrm{S/m}$. At the chosen frequency these parameters corresponded to a wavelength of approximately $\lambda = 860\,\mathrm{m}$. We note that the geometric dimensions are typical for many under-water ranging procedures and the chosen propagation parameters are reasonably representative of a sea-water environment.

Our objective for these experiments were two fold; firstly we investigated whether the FISTA method was able to resolve the positions of the dipole sources. To assess this in a meaningful way we need to define the discrete point-spread function (PSF) $\chi(\vec{y}_i)$. We define the PSF at a position $\vec{y}$ on the surface Γ_s as the total magnitude of the reconstructed dipole moments,

$$\chi(\vec{y}_i) = \left(|\vec{m}_i|^2 + |\vec{e}_i|^2\right)^{1/2}. \tag{19}$$

We say that a source can be identified in the PSF image if an identifiable cluster is present with a clearly defined centroid (point of highest magnitude). The degree of which two sources in the PSF are resolved relates to the degree that two clusters overlap. Ideally two sources would be clearly resolved if the two clusters are non-overlapping. The second objective for these experiments was to determine whether relevant physical features of the dipole sources could be effectively reconstructed. More specifically, these features include the type of dipole (electric or magnetic), its orientation, and its position on Γ_s. To visualize this in a clear and concise manner, for each reconstructed electric and magnetic dipole distribution we plot a phase-shifted dipole moment (PSDM) image which plots the real part of a phase-shifted complex amplitude of each of the tri-axial component of a dipole moment as a function of position. That is we find the point $\vec{y} = (x_0, y_0)$ on the plane Γ_s corresponding to the maximum phase angle θ_0 over the three components of the dipole moments. The complex amplitudes are then phase shifted with angle θ_0 and only the real part of each tri-axial vector is displayed.

We discuss the major points regarding the experiments below, but for convenience to the reader we summarize the numerical experiments in Table 1. The table lists the type and orientation of both sources for each experiment. The column labeled "resolved" indicates whether or not the ℓ_1 approach was able to detect two separate dipole clusters in the PSF. The column labeled "reconstructed" indicates whether the orientation and dipole type of each of the sources was correctly ascertained in the PSDM images.

Table 1. Summary of ℓ_1 numerical experiments for reconstructing two dipole sources.

| Experiment #	δ	Type	Orientation	Type	Orientation	Resolved?	Reconstructed?
1	$10\,\mathrm{m}$	Magnetic	Z	Magnetic	Z	Yes	Yes
2	$5\,\mathrm{m}$	Magnetic	Z	Magnetic	Z	No	N/A
3	$5\,\mathrm{m}$	Magnetic	X	Magnetic	Z	Yes	Yes
4	$2\,\mathrm{m}$	Magnetic	X-Y	Electric	Z	Yes	Yes

4.1. Comparison of ℓ_1 with ℓ_2 Methods

In the first experiment, which we refer to as experiment 1, we show some basic differences between ℓ_1 and ℓ_2 approaches. We chose a value of $\delta = 10\,\mathrm{m}$ as the spacing between two Z oriented magnetic dipoles. This corresponded to a spacing of approximately 0.011λ between the two sources. For the ℓ_2 reconstructions we chose an LSQR iterative regularization method where the stopping rule is chosen according to the noise level as discussed in [16]. The FISTA method was run with a regularization parameter of $\alpha = 0.1$ which was chosen heuristically.

(a) LSQR   (b) FISTA
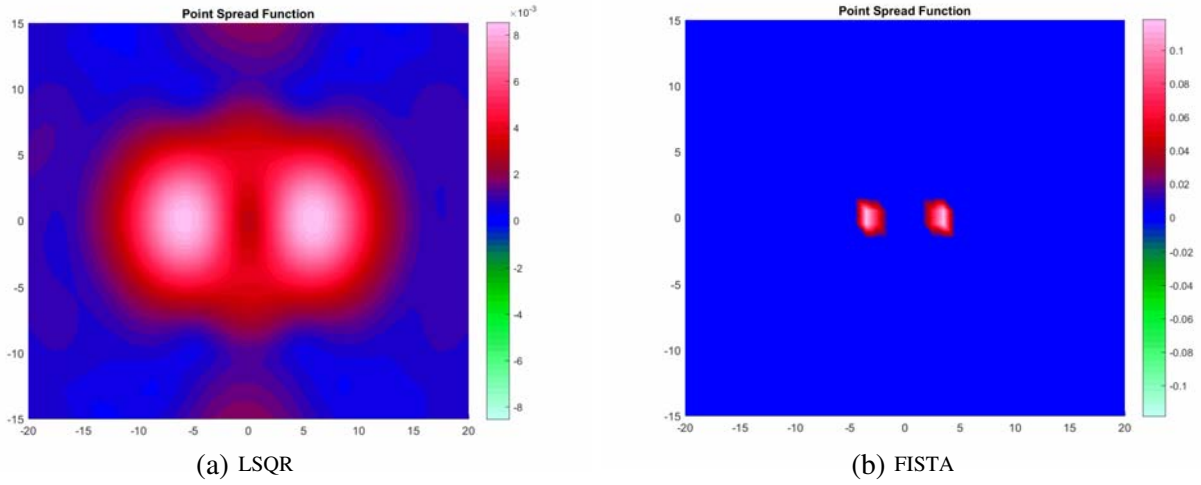
Figure 4. The PSFs for experiment 1 reconstructed by the LSQR (ℓ_2 regularization) and FISTA (ℓ_1 regularization) methods.

Figure 4 shows plots of the PSF for the LSQR and FISTA approaches. As expected the PSF for the FISTA reconstruction clearly exhibits superior resolution of the two sources with no overlap between the two clusters. On the other hand, the LSQR exhibits a blurrier image of the sources with observable ringing effects throughout the image plane. Looking at the PSDM plots reconstructed by the LSQR method and shown in Figure 5, we can observe that indeed a stronger preference for a magnetic dipole decomposition is visible in the reconstruction. However the electric dipole distribution is not identically zero as one would expect in this particular experiment. Furthermore the orientations of the reconstructed magnetic dipole moments in 5(b) is inconsistent with the physical nature of the sources. In comparison, Figure 6 shows magnetic dipole PSDM obtained using the FISTA approach, where we

(a)

(b)
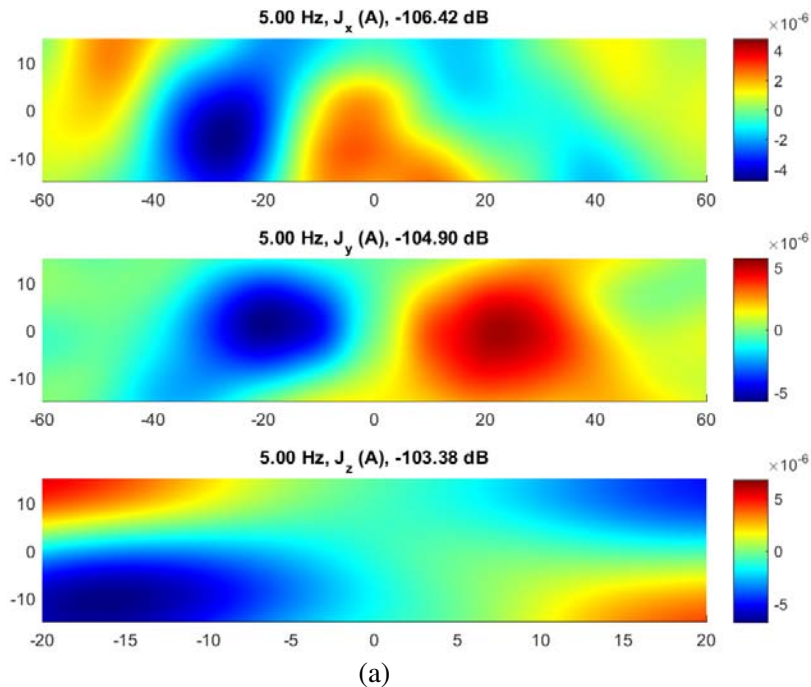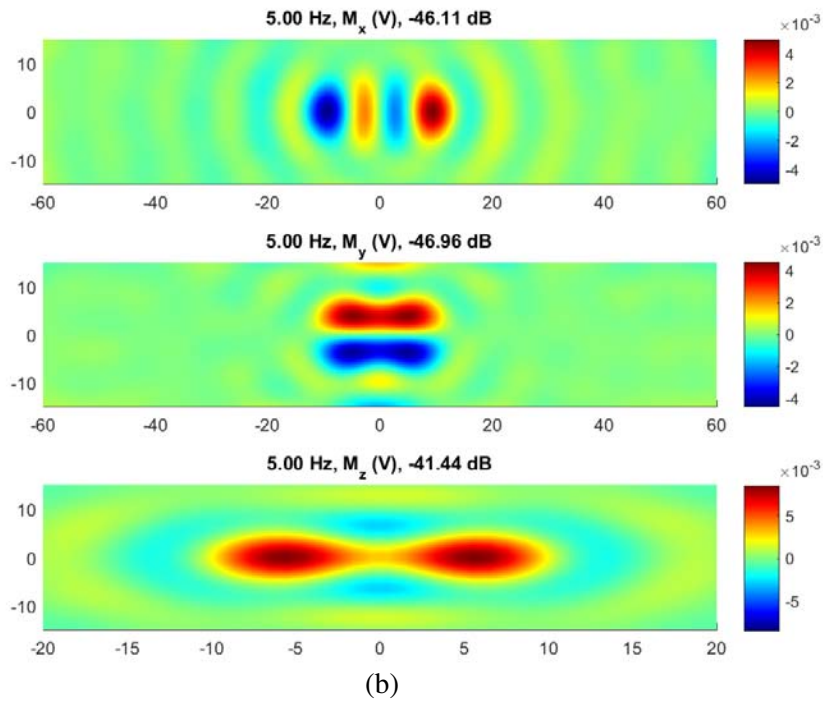
Figure 5. Showing the PSDM image for both electric and magnetic dipole moments reconstructed by the LSQR method for experiment 1. The physical nature and orientation of the sources is not very apparent. (a) Electric dipoles. (b) Magnetic dipoles.
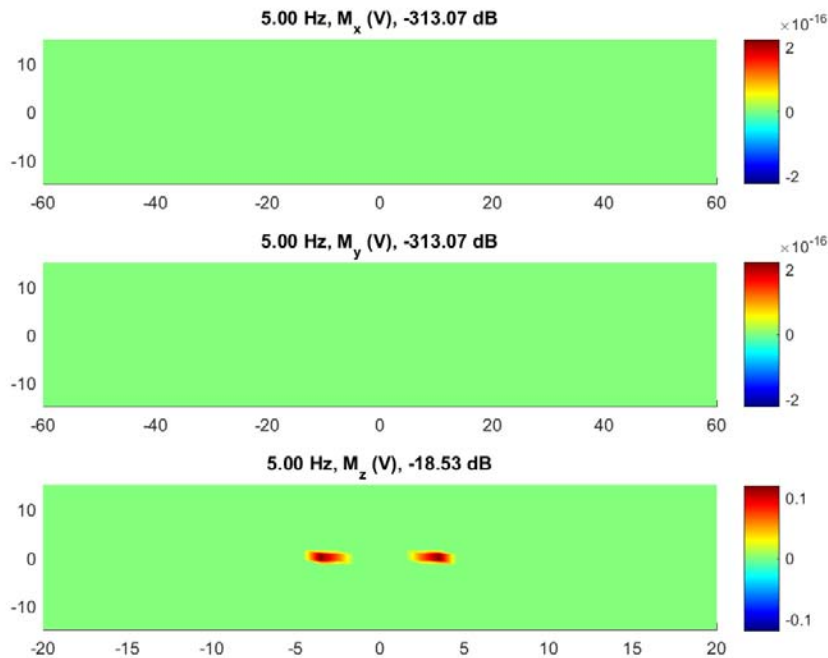

Figure 6. Showing the PSDM image for magnetic dipoles reconstructed by the FISTA method for experiment 1. The two Z-oriented magnetic dipoles placed at $x = -5$ and $x = 5$ are clearly resolved with virtually no ambiguity.

observe the presence of two purely Z oriented sources. The electric PSDM for the FISTA method was not shown here since they amplitudes were identically zero as expected.

4.2. Source Polarization Experiment

Experiments 2 and 3 illustrate an interesting behavior using the FISTA reconstruction approach. Our numerical experiments indicated that when we decreased the δ parameter to a value smaller than $10\,\mathrm{m}$ for two similarly oriented dipole sources, the FISTA reconstructions would yield single dipole distributions at an averaged position of the two sources. As an example, we consider for experiment 2 two magnetic dipole sources both oriented in the Z direction but spaced $\delta = 5\,\mathrm{m}$ apart. This corresponded to a separation of approximately 0.005λ. Figure 7 shows the resulting magnetic PSDM image for the FISTA method. Here we observe a single Z-oriented source reconstructed at the location of $x = 0$, i.e., the averaged position of the two sources. A natural question arises then, at least in the context of this numerical experiment, is $10\,\mathrm{m}$ a resolution limit of the ℓ_1 regularization approach for this particular wavelength? To attempt to answer this question, numerical experiment 3 used the same $\delta = 5\,\mathrm{m}$ spacing but the magnetic dipole sources had different polarities. The first dipole is chosen with a polarity aligned with the X axis and we keep the second dipole oriented along the Z axis. Here we see in Figure 8 where the reconstructed magnetic PSDM image shows the two sources are resolved each with the correct orientation. We believe this discrepancy between experiment 2 and 3 can be attributed to the nature of the penalty term imposed in the regularization procedure. In experiment 2 the two dipoles are spaced (relatively) close to each other. Without additional diversity in the data (different orientation, frequency, or dipole type) an ambiguity exists to whether this is a single source or two sources, as both models would equally satisfy the data. Thus imposing sparsity would cause the single dipole solution to be favored. However when additional diversity exists in the data this is no longer the case.
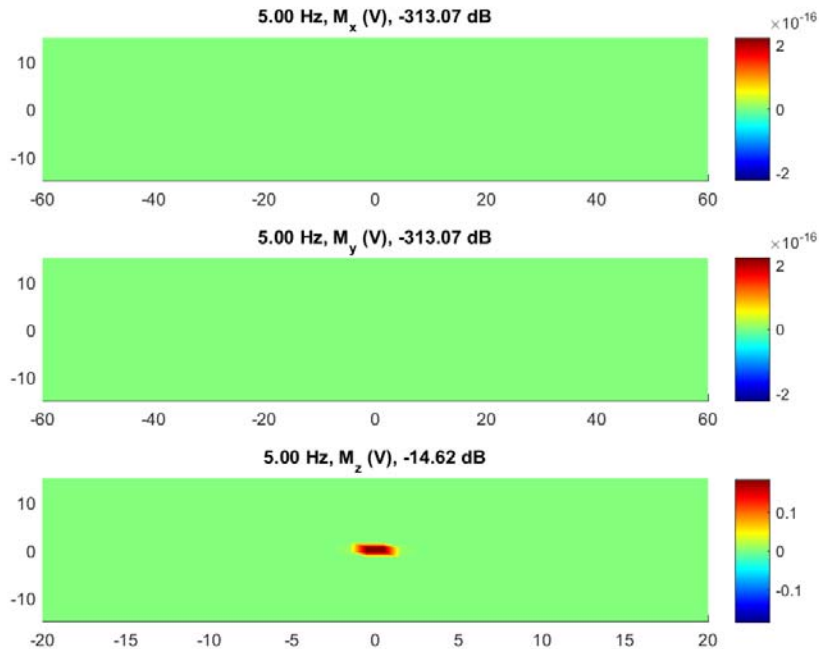
Figure 7. PSDM of the FISTA reconstruction for experiment 2 where a single source at $x = 0$ was identified rather than two magnetic dipole sources.
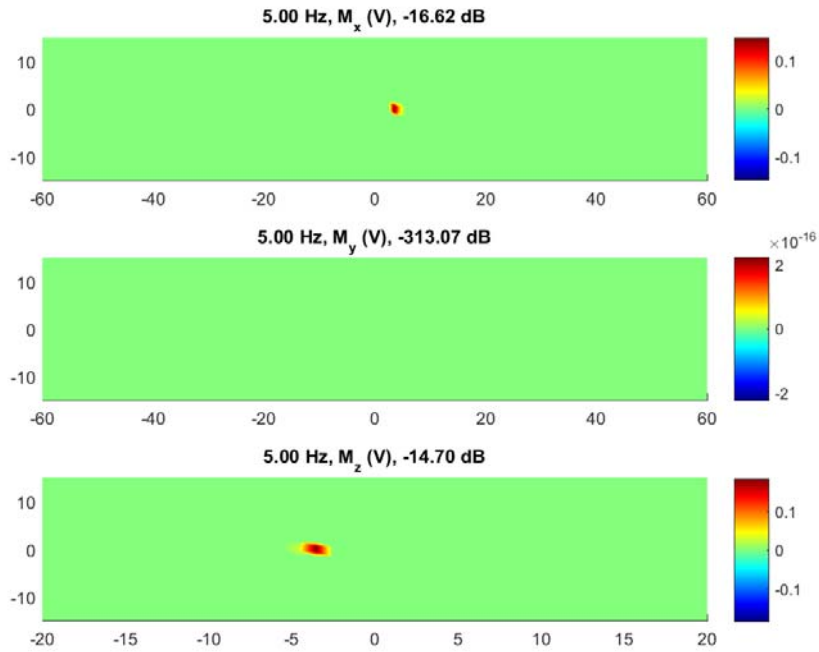
Figure 8. Magnetic PSDM image for experiment 3. The positions and orientations were correctly identified by the FISTA method.

4.3. Identification of Dipole Type

In experiment 4 we illustrate proof of concept to our hypothesis that sparsity is an effective prior to mitigate the non-uniqueness issue of the dual-source approach. In this experiment we used a single magnetic dipole $\vec{m} = (\frac{1}{\sqrt{2}}, \frac{1}{\sqrt{2}}, 0)$ and a single electric dipole source aligned with the Z axis. Again both sources were spaced $\delta = 2\,\mathrm{m}$ from each other along the X axis. The FISTA reconstructions shown in Figure 9 indicate that both dipole sources are resolved in the reconstruction. Furthermore the correct orientations and polarities of each dipole source source was faithfully reconstructed.

5. PHYSICAL EXPERIMENTS: TNO COIL POSITIONING WITH EARTH FIELD SIMULATOR (EFS) MAGNETIC DATA

In this section we consider the sparse source imaging approach for localizing sources from AC magnetic field data obtained at an EFS facility in Schirnau, Germany [14]. The EFS data discussed here was part of a larger set of multi-national effort of experiments known as the Radar Infrared electroMagnetic Pressure and Acoustic Ship Signature Experiments (RIMPASSE) during 2011 using a Canadian research vessel known as the CFAV Quest. The EFS facility (see Figure 10) is equipped with various coils (see Figure 10) which are capable of simulating various magnetic conditions that a vessel may experience in various parts of the world. The experiments conducted at the EFS facility involved mostly magneto-static ranging for the purposes of understanding the response of the Quest to various magnetic field conditions and calibrating on-board degaussing systems. However a number of runs using AC current through coils on-board the CFAV Quest. The particular AC sources that we consider in this work are denoted as the TNO or "Dutch" coil and the DRDC or "Canadian" coil. A more complete description of the coils and amplifier specifications are detailed in [14]. The Dutch coil shown in Figure 11 was oriented in various ways through-out the experiments. For the presented experiments the TNO coil was positioned at about $2\,\mathrm{m}$ forward of the vessel shaft, $3.8\,\mathrm{m}$ port (left) of the ship center line, and about $2.4\,\mathrm{m}$ below the waterline. The Canadian coil was positioned within $2\,\mathrm{m}$ of the Dutch coil on the same plane.

Table 2. Summary of the EFS run numbers under consideration in this work.

Run #	Dutch Coil Orientation	Canadian Coil Orientation	Frequency	Sampling Rate
1561	Y	-	2 Hz	20 Hz
1564	X	-	2 Hz	20 Hz
1566	X	Z	2 Hz	20 Hz

The magnetic field is measured using two planar sensor arrays at depths of 9 m and 13 m respectively which are installed directly below the ship's position with each plane consisting of 379 tri-axial magnetometer nodes for a total of 758 sensing elements. The exact positioning of the sensing elements and the ship's position within the EFS with respect to a single plane are shown in Figure 12. It is important to note that the 9 m sensor array is installed on the sea floor while the sensor array at 13 m depth is installed within the seafloor. A Cartesian coordinate system using reference location G0 is setup on each plane where the X direction is along the longitudinal axis and extends from 0 to 94 m. The Y axis is along the latitudinal direction and ranges from -18 m to 18 m. In reference to the sensor coordinates shown in Figure 12 the Dutch coil corresponded to position I12 which is given in local coordinates as (28, 4). Similarly the Canadian coil was positioned positioned at I11 with coordinates (26, 4). Both coils were on a plane approximately 6.6 m above the 9 m plane.

We employed a plane to plane NEH approach in this work using the run numbers specified in Table 2. The sensor array located at 9 m depth served as the measurement surface Γ_m and a source plane Γ_s was placed 6.6 m above Γ_m. The source plane coincided to the plane for which the coils were approximately positioned. To obtain the signature of the ship for a given run, a reference run is taken with no vessel present in the EFS. A subsequent measurement is then taken with the CFAV QUEST present in which case the reference is subtracted yielding only the ship's magnetic signature which is the magnetic flux density ($\vec{B}$ field) measured in units of nT. The multiple sensors required to form the hologram are sampled in the time domain. Relative phase information between the sensor channels, critical for hologram formation, can be obtained due to the fact that the sensors are time locked, that is, synchronously sampled. Due to this there also is no need for a reference sensor, the latter being necessary when the data from different channels is not sampled simultaneously as is often

(a)

(b)
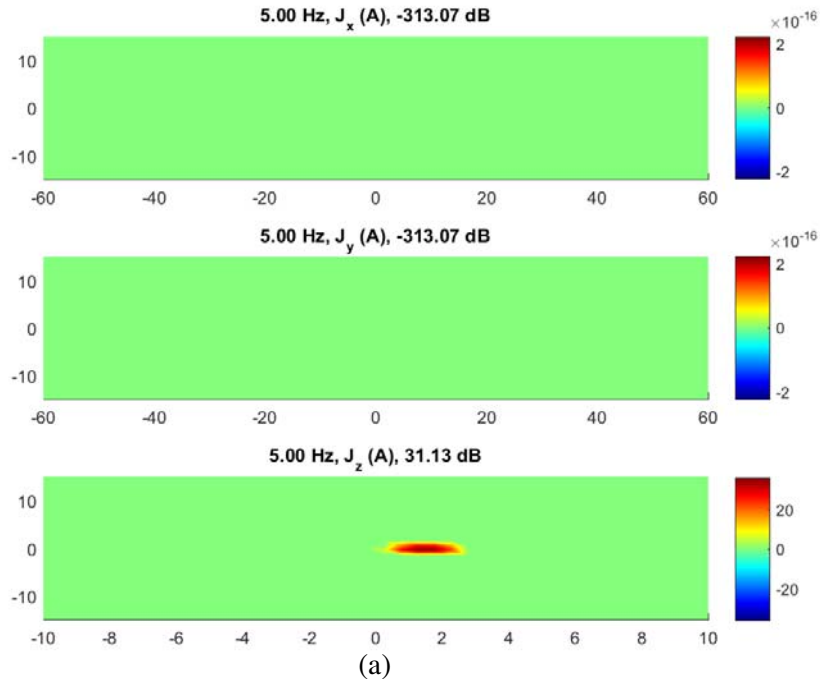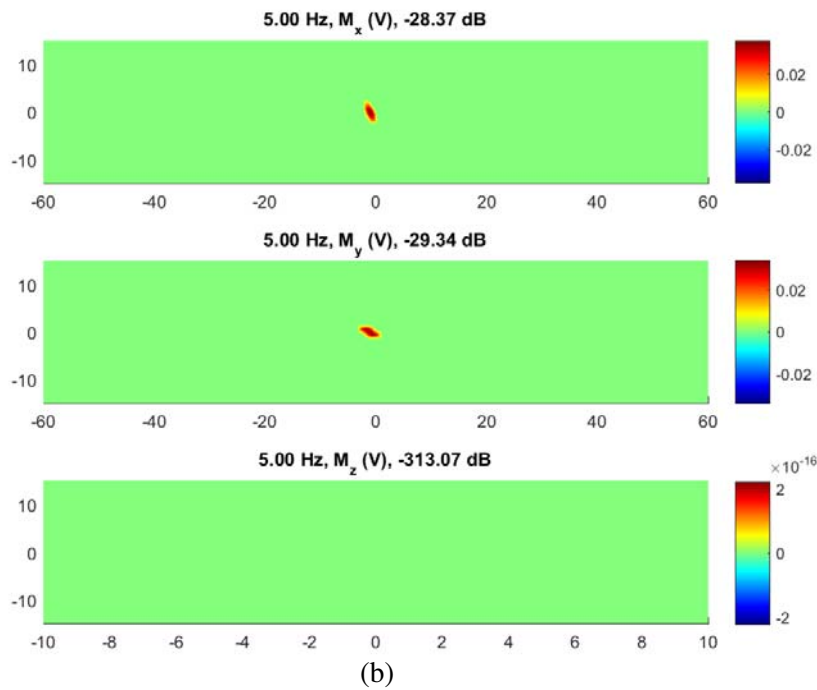
Figure 9. Electric and magnetic PSDM images for experiment 4. The FISTA method was able to distinguish between electric and magnetic dipole sources as well as preserve their orientations and positions. (a) Electric dipoles. (b) Magnetic dipoles.

Figure 10. The EFS facility at Shirnau, Germany.

the case in nearfield acoustical holography (see [17, 18]). The time-domain magnetic flux density data is then converted into units of A/m and Fourier processed to yield the frequency components of the hologram data. A magnetic field hologram at approximately 2 Hz was then extracted for all three runs and used as the input data for the proposed compressive NEH procedure. We note that we used a free-space Green's function where as a Green's function that takes into account reflections along the seafloor-water interface at 9 m depth would theoretically be more accurate. However we leave NEH with incorporation of a layered Green's function approach for future work. Figures 13, 14, and 15 show the phase-shifted magnetic field holograms and the resulting magnetic dipole PSDM images for each of the runs respectively. The phase shifted images are as described in Section 4. We note that only the magnetic PSDM images are shown since again the resulting electric dipole moments were determined to be identically zero by the reconstruction algorithm. This is not a surprising result since a coil driven with an AC electric current source on these scales is effectively modeled by a radiating magnetic dipole. Consequently we see that a sparsity prior is very useful for model reduction techniques. Looking

Figure 11. Illustration of the Dutch coil under a Z orientation setup.
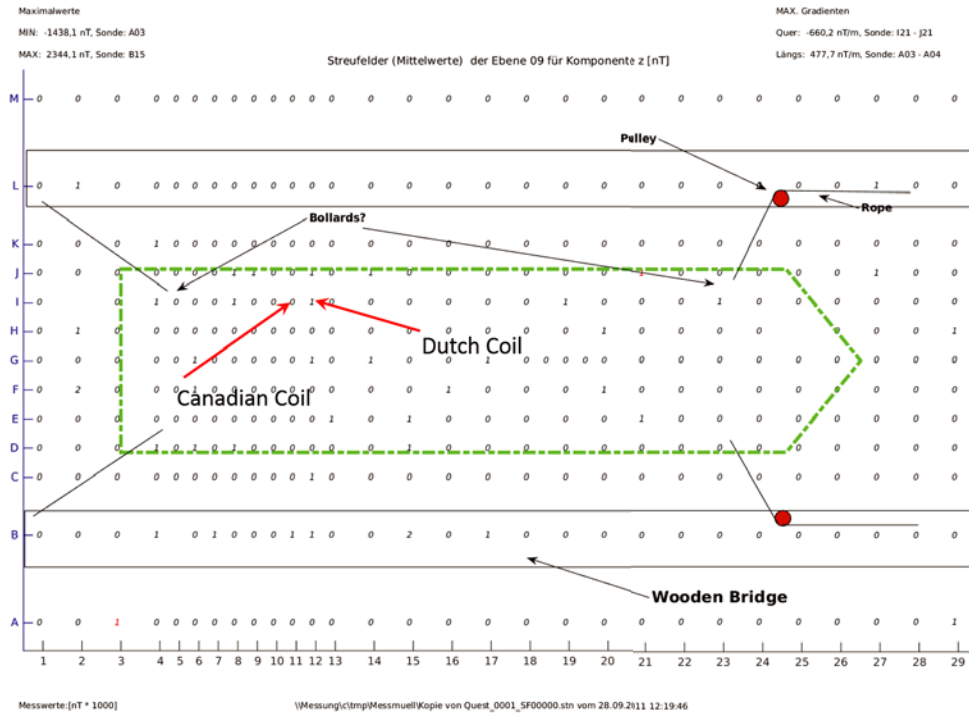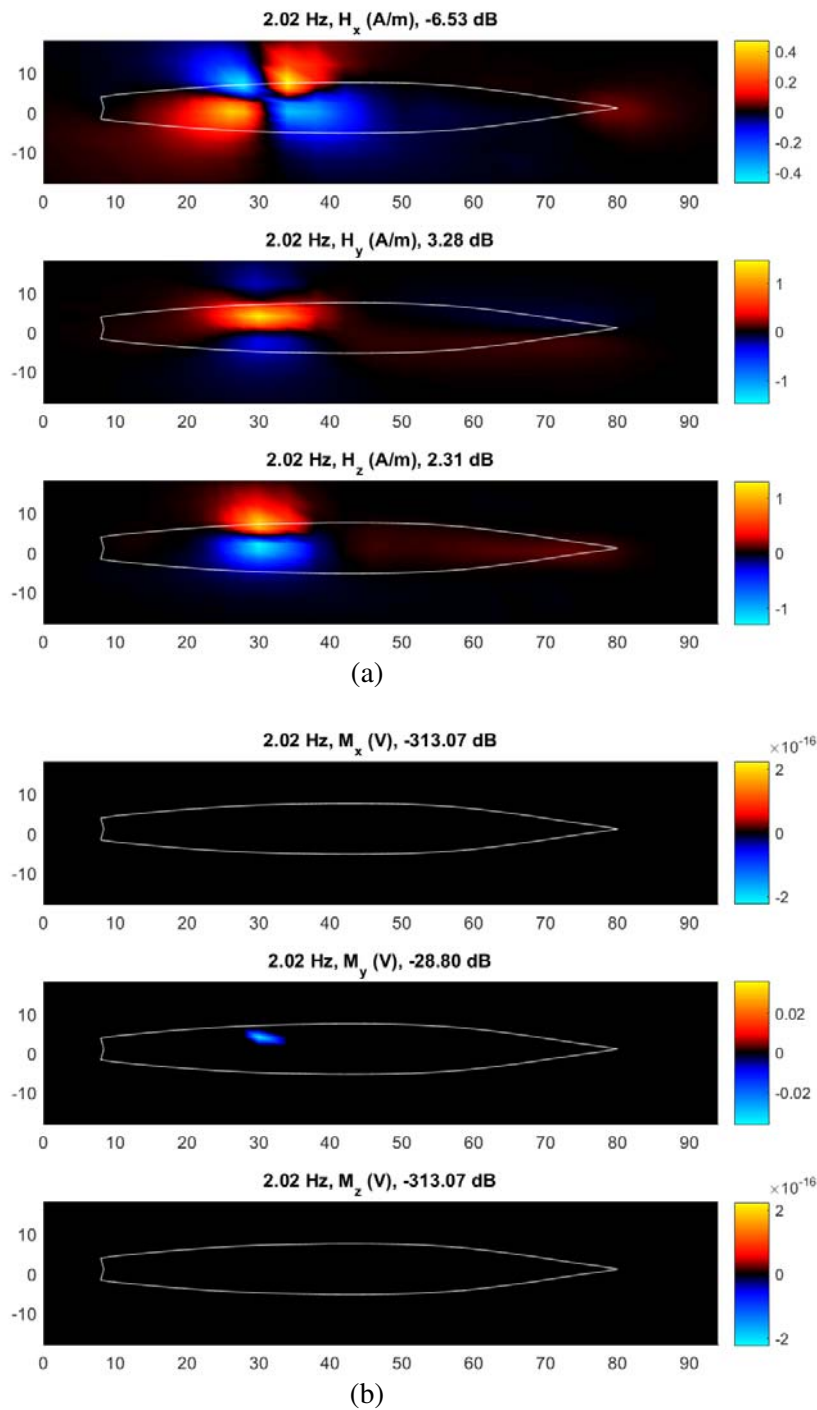

Figure 12. Geometry of the EFS experiments. Here the position of the static ship is shown with respect to the EFS sensor array. The Dutch coil is located at sensor location I12 and the Canadian coil is located at sensor location I11. This corresponded to a separation distance of $2\,\mathrm{m}$ between the two coils.
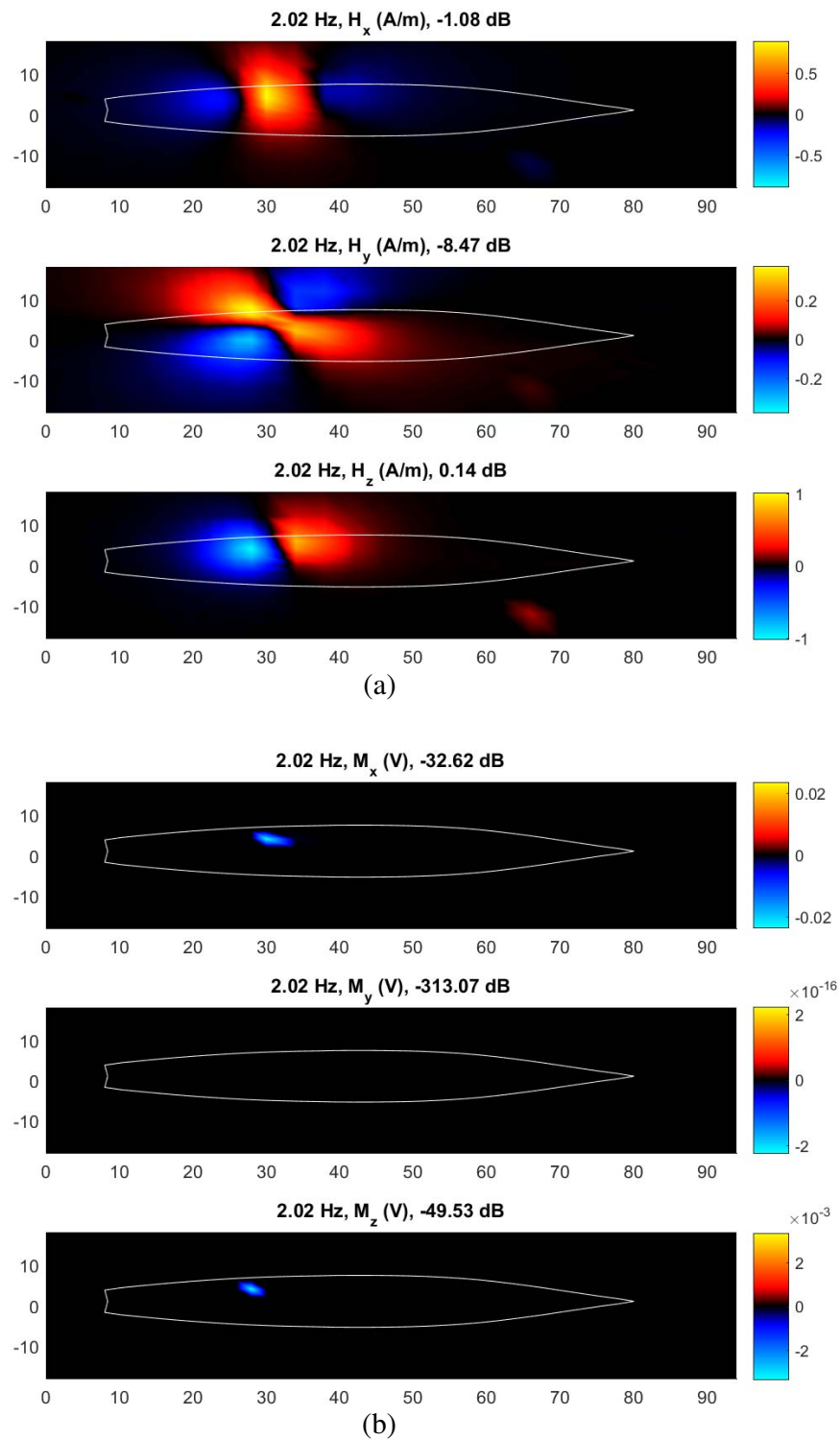
(a)

(b)

Figure 13. Extracted near-field magnetic field hologram at 2 Hz and the resulting magnetic PSDM image for run 1561. (a) Magnetic field hologram at 9 m depth. (b) Reconstructed magnetic dipole sources at 6.6 m depth.

specifically at Figures 13 and 14, which corresponded to runs where only the Dutch coil was actively driven but with different orientations as labeled in Table 2. Again we see that the method is successful at determining the correct orientations of the coil. In both cases the highest amplitude of the energy was determined to be at the position (30, 4) which was 2 m away from the documented positioning

(a)

(b)
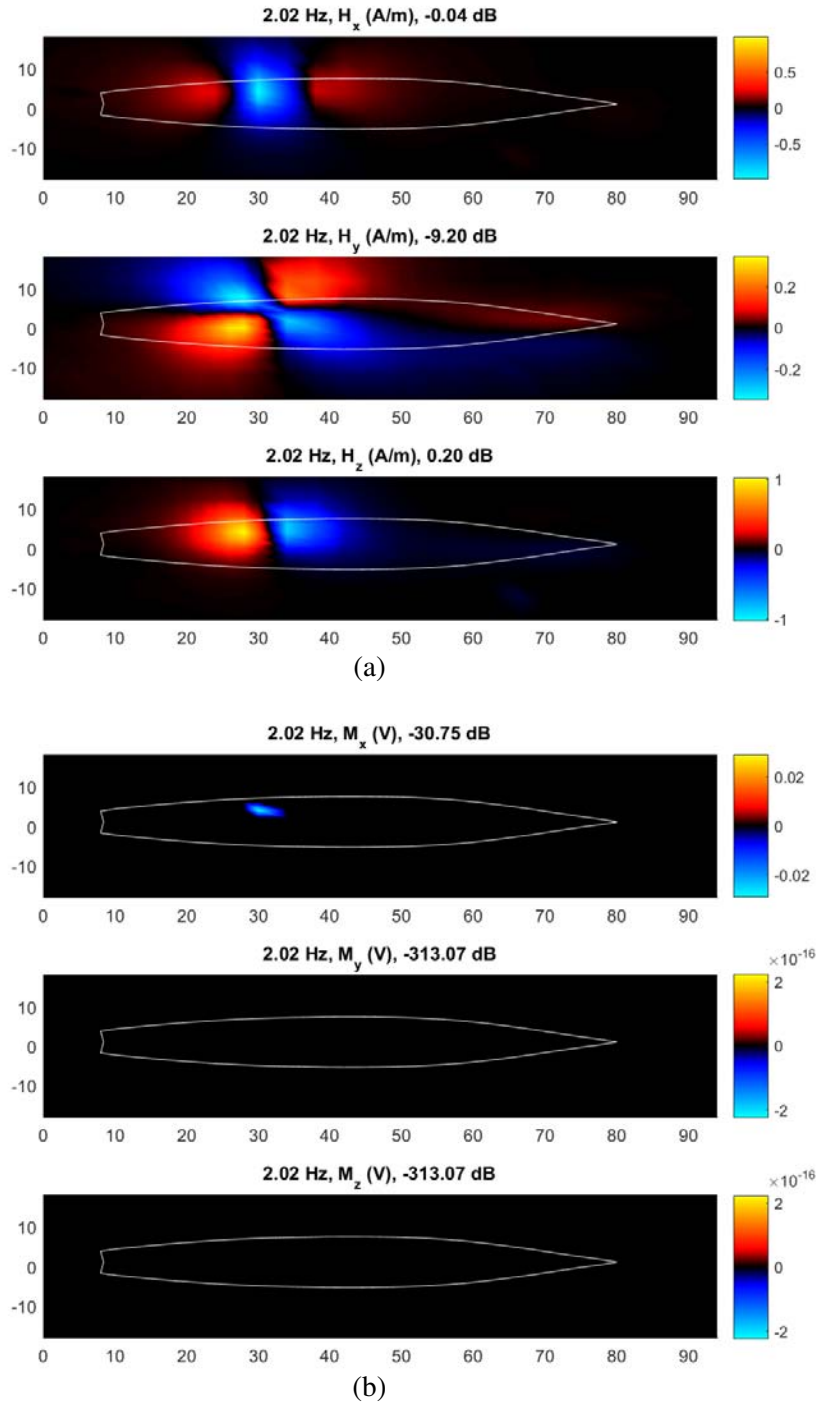
Figure 14. Extracted near-field magnetic field hologram at 2 Hz and the resulting magnetic PSDM image for run 1564. (a) Magnetic field hologram at 9 m depth. (b) Reconstructed magnetic dipole sources at 6.6 m depth.

of the coil. Figure 15 shows the results corresponding to the case where both Dutch and Canadian coils were actively driven. Here we can clearly see the presence of two magnetic dipoles placed within 2 m (0.0015λ) of each other along the X axis and their respective orientations were correctly identified. These results correlate well with the conclusions of the numerical study presented above.

Figure 15. Extracted near-field magnetic field hologram at 2 Hz and the resulting magnetic PSDM image for run 1566. (a) Magnetic field hologram at 9 m depth. (b) Reconstructed magnetic dipole sources at 6.6 m depth.

6. FINAL REMARKS

In this paper we presented a source reconstruction technique based on a sparse electric and magnetic dipole decomposition for the purpose of back-projecting near-field electromagnetic to a source surface within an infinite underwater background medium. While the presented approach focused on use of ℓ_1 techniques for not only increasing source localization resolution, but also preservation of important physical features of the dipole sources, we do note that the presented technique is also suitable for accurately predicting of far-field behavior.

The presented numerical and physical experiments indicated a number of important implications concerning electromagnetic source reconstruction techniques. The first implication is related to the non-unique nature of the combined vector potential approach. As discussed above the only requirement imposed on the electric and magnetic currents is that they provided an equivalent representation of the observations. We gave a simple example illustrating that ℓ_2 techniques without any additional constraints in general fail to provide equivalent sources that relate to physical sources that may be present on Γ_s. On the other hand we witnessed from the numerical experiments that the sparse regularization approach produced reconstructions that corresponded to a high degree to the physical nature of the sources. Indeed the sparse regularization approach not only gave a clear indication of the type of source (magnetic or electric dipole) but also was able to clearly identify the correct orientations. Our argument for this difference in behavior is based on an Occam's razor hypothesis. The ℓ_2 approach only demands smoothness in the reconstructed dipole moments whereas we can think of the ℓ_1 approach as demanding sparsity or simplicity in the solution which in the case of a localized source proves to be a better mitigating constraint for the non-uniqueness issue. This hypothesis was also supported by the EFS experiments where the physical nature of the coils (type, position, and orientation) were almost perfectly reconstructed. The second implication concerns the super-resolution capability of near-field electromagnetic holography. We argued that regularization is a major factor governing the ability to resolve sources when back-projecting near-field surface data. This was clearly demonstrated with the presented numerical experiments comparing the ℓ_2 and ℓ_1 approach. However we also witnessed an interesting phenomenon in the ability to resolve two magnetic dipoles with the ℓ_1 approach. More specifically we presented a case where the method failed to resolve two magnetic dipoles radiating a field at 5 Hz with the same orientation placed within 5 m of each other. We however showed that this was not a resolution limit but a consequence of the regularization method's demand for simplicity, since if the two sources contained additional distinctions (polarity and physical type) the approach was able to clearly resolve them all the way to the resolution of the source grids. Again further proof of concept of this hypothesis was given in the the EFS experiments where the Dutch and Canadian coils driven at 2 Hz were resolved within 2 m (0.004λ) of each other.

There is good potential for future investigation of the presented work. We mentioned incorporation of Green's functions that can account for interface boundaries in an effort to improve reconstruction accuracy. Also the results of this work can be incorporated for the purpose of future automated diagnostic and non-destructive evaluation purposes that can leverage the robustness of the ℓ_1 reconstruction for identifying the physical features of the sources.

REFERENCES

1. Alqadah, H. F., N. Valdivia, and E. G. Williams, "A super-resolving near-field electromagnetic holographic method," *IEEE Transactions on Antennas and Propagation*, Vol. 62, No. 7, 3679–3692, Jul. 2014.
2. Balanis, C. A., *Antenna Theory: Analysis and Design*, Wiley-Interscience, 2005.

3. Beck, A. and M. Teboulle, "A fast iterative shrinkage-thresholding algorithm for linear inverse problems," *SIAM Journal of Imaging Sciences*, Vol. 2, 183–202, 2009.

4. Candes, E., "Compressive sampling," *International Congress of Mathematics*, 2006.

5. Candes, E., "The restricted isometry property and its implications for compressed sensing," *Comptes Rendus Mathematique*, Vol. 346, No. 9–10, 589–592, May 2008.

6. Colton, D. and R. Kress, *Inverse Acoustic and Electromagnetic Scattering Theory*, Springer, 1998.

7. Donoho, D., "For most large underdetermined systems of linear equations, the minimal ell-1 norm solution is also the sparsest solution," *Communications on Pure and Applied Mathematics*, Vol. 59, 797–829, 2006.

8. Hansen, P. C., *Rank-deficient and Discrete Ill-posed Problems*, SIAM, Philadelphia, 1998.

9. Harrington, R. F., *Time-harmonic Electromagnetic Fields*, Wiley-IEEE Press, 2001.

10. Holmes, J., *Reduction of a Ship's Magnetic Field Signatures*, Morgan & Claypool Publishers, 2008.

11. Izquierdo, J., J. Rubio, J. Corcoles, and R. Gomez-Alcala, "Efficient radiation antenna modeling via orthogonal matching pursuit in terms of infinitesimal dipoles," *IEEE Antennas and Wireless Propagation Letters*, 99:1-1, 2015.

12. Morgan, M. A., "Electromagnetic holography on cylindrical surfaces using k-space transformations," *Progress In Electromagnetics Research*, Vol. 42, 303–337, 2003.

13. Natarajan, B. K., "Sparse approximate solutions to linear system," *SIAM J. Comput.*, Vol. 24, No. 2, 227–234, 1995.

14. Bradley Nelson, J., T. C. Richards, M. Birsan, and C. Greene, "Rimpasse 2011 electromagnetic trials quick-look report," *Technical Report*, Defence R&D Canada-Atlantic, 2011.

15. Quijano, J. L. A. and G. Vecchi, "Field and source equivalence in source reconstruction on 3D surfaces," *Progress In Electromagnetics Research*, Vol. 103, 67–100, 2010.

16. Valdivia, N., E. G. Williams, P. C. Herdic, and B. Houston, "Surface decomposition method for near-field acoustic holography," *Journal of Acoustical Society of America*, 2012.

17. Valdivia, N. P. and E. G. Williams, "The reconstruction of surface tangential components of the electromagnetic field from near-field measurements," *Inverse Problems*, Vol. 23, 2007.

18. Valdivia, N. P. and E. G. Williams, "Study of the comparison of the methods of equivalent sources and boundary element methods for near-field acoustic holography," *The Journal of the Acoustical Society of America*, Vol. 120, No. 6, 3694–3705, 2006.

19. Williams, E. G. and J. D. Maynard, "Holographic imaging without the wavelength resolution limit," *Phys. Rev. Lett.*, Vol. 45, 554–557, Aug. 1980.

20. Williams, E. G., *Fourier Acoustics: Sound Radiation and Nearfield Acoustical Holography*, Academic Press, London, U.K., 1999.

21. Williams, E. G. and N. P. Valdivia, "Near-field electromagnetic holography in conductive media," *IEEE Transactions on Antennas and Propagation*, Vol. 58, No. 4, 1181–1192, 2010.